Lab on a Chip

PAPER

View Article Online
View Journal | View Issue

Cite this: *Lab Chip*, 2023, **23**, 2808

Rock-on-a-chip: "Seeing" the association/disassociation of an adaptive polymer in solutions flowing through porous media†

Yan Zhang,[ab] Xuezhi Zhao,[a] Peihui Han,[c] Tianlei He,[b] Hongyao Yin,[a] Liyuan Zhang,*[bd] Yujun Feng *[a] and David A. Weitz *[b]

The flow and transport of polymer solutions through porous media are ubiquitous in myriad scientific and engineering applications. With escalating interest in adaptive polymers, understanding the flow dynamics of their solutions is indispensable (yet lacking). Here, the hydrophobic-effect-driven reversible associations in a self-adaptive polymer (SAP) solution and its flow characteristics in a microfluidic-based "rock-on-a-chip" device have been analyzed. The hydrophobic aggregates were fluorescent labeled; this enabled a direct visualization of the *in situ* association/disassociation of the polymer supramolecular assemblies in pore spaces and throats. Furthermore, the influence of this adaptation on the macroscopic flow behavior of the SAP solution was analyzed by comparing its flow with that of two partially-hydrolyzed polyacrylamide (the molecular weight (MW)-equivalent HPAM-1 and ultrahigh-MW HPAM-2) solutions in the semi-dilute regime with similar initial viscosities. At low flow rates (with shear predominance), the SAP solution showed a low shear viscosity compared to HPAM-1, indicating a higher shear susceptibility for association than chain entanglement. Although the SAP exhibited the same elastic instability as the non-adaptive polymers above a threshold flow rate, the adaptable structure of the former advanced the onset of its viscoelastic-governed flow, providing a stronger flow resistance, possibly through an extension resistance. Furthermore, 3D-media analysis indicated that the reversible association/disassociation of SAP increased the accessible pore space during nonaqueous-liquid displacement, facilitating oil production.

Received 23rd January 2023,
Accepted 15th May 2023

DOI: 10.1039/d3lc00068k

rsc.li/loc

Introduction

Diverse scientific and industrial processes, such as, filtration,[1] chromatography,[2] microfluidics,[3] fiber spinning,[4] enhanced oil recovery,[5,6] and groundwater remediation,[7] involve the flow of polymer solutions through porous media. The pore structure and polymer properties influence the transportation dynamics. For over half a century, numerous investigations have concentrated on conventional linear polymers, including polyacrylamide (PAM),[8] partially hydrolyzed polyacrylamide (HPAM),[9–15] polyethylene oxide (PEO),[16] and polystyrene.[17] However, recent studies have analyzed functional polymers (such as the adaptive versions of conventional polymers), rapidly increasing their utilization in the aforementioned fields.[18–22] Thus, the flow characteristics of such polymer solutions within porous media (including a direct validation of their reversible adaptive behavior) requires intensive investigation.

Adaptive polymers exhibit dynamic constitutional chemistry, *i.e.*, their molecular components are linked through changeable covalent bonds and noncovalent interactions (such as, hydrogen bonds, hydrophobic interactions, and π–π stacking)[20,23–30] that form and break reversibly. Thus, the aggregate structures of these polymers undergo flexible modifications by spontaneous assembly/disassembly in the presence of physical/chemical stimuli and environmental changes. Consequently, unlike conventional polymers, adaptive materials exhibit numerous macroscopic features, such as self-healing[31–33] and reversible property-transitions (including modifications in their apparent

[a] *Polymer Research Institute, State Key Laboratory of Polymer Materials Engineering, Sichuan University, Chengdu 610065, China. E-mail: yjfeng@scu.edu.cn*
[b] *School of Engineering and Applied Sciences, Harvard University, Cambridge, MA 02138, USA. E-mail: liyuanzhang@seas.harvard.edu, weitz@seas.harvard.edu*
[c] *EOR Laboratory, Exploration & Development Research Institute, Daqing Oilfield Company, PetroChina, Daqing 163712, China*
[d] *School of Petroleum Engineering, China University of Petroleum, Qingdao 266580, China*

† Electronic supplementary information (ESI) available: Raw data of fluorescence emission spectra; the stress-relaxation characterization of polymer solution; the flow pressure drop data and shear rate distribution when polymer solution flowing through 2D micromodel; the physical parameter characterization of 3D porous medium and oil displacement results within it. Supplementary videos of the dynamic mixing process of ANS and SAP solution, average vector fields in 2D micromodel, and oil saturation and displacement processes in 3D porous media. See DOI: https://doi.org/10.1039/d3lc00068k

viscosity, phase state, and surface, interfacial, and shape morphology).[22,34–36] However, the influence of these adaptive phenomena on the flow of adaptive polymers through porous media, including their influence on macroscopic transport, remains unverified.

Theoretically, when the energy of a specific volume of polymer solution suffering from pore-throat is greater than that of its weak noncovalent linkages (generally less than 100 kJ mol^{-1})[37] and less than that of its C–C covalent bonds (approximately 346 kJ mol^{-1} on an average),[38] disassembly can occur in the polymer, without irreparable destruction. Subsequently, if the energy of polymer suffering from pore space is less than that of the weak contacts in the polymer, the assemblies could rebuild and recover their macroscopic attributes. As a result, the occurrence of adaptive association/disassociation behavior is governed by the exact energy of polymer suffered in solution flow, which can be determined using the *in situ* stress (energy/volume); however, the stress distribution in polymer solution flow has not been quantified in previous publications.

On the other hand, the highly random structures and opacity of realistic media make the direct visualization of *in situ* adaptation very challenging. Micromodels with 2D and 3D geometries (fabricated using optically-transparent polymers and glass beads) can overcome this limitation. Tuning the polymer solution and medium refractive index values enables a pore-level observation of the flow and fluid structures under transient conditions.[39–42] Experimentation with 2D-media models[5,6,43,44] show that the flow resistance values of traditional polymer solutions increase abruptly beyond a threshold flow rate, indicated by an increase in their local effective viscosity (η_{eff}), with their bulk shear viscosity in the shear-thinning regime. Recently, Browne and Datta[13] have reported a similar phenomenon in a disordered 3D model. Although studies with common polymer solutions yield powerful insights into their flow dynamics, these polymers differ in molecular composition, aggregate structure, and stress response from adaptive polymers. Thus, further studies are required to confirm whether adaptive polymer solutions exhibit flow properties similar to those exhibited by conventional polymers.

In this study, a hydrophobically driven self-adaptive polymer (SAP, 8.7 × 10^6 g mol^{-1}) containing C_{12}-tailed hydrophobic comonomers as pendant grafts (to facilitate hydrophobic association) has been investigated; additionally, its flow has been compared to that of a molecular weight (MW)-commensurate reference, HPAM-1 (8.2 × 10^6 g mol^{-1}), and an ultrahigh-MW counterpart, HPAM-2 (24.9 × 10^6 g mol^{-1}) (Table 1). According to a previous publication,[22] an adaptive association/disassociation transition of SAP chains occurs during the completely reversible bulk-solution viscosity change of the SAP in response to shear forces. In this study, the SAP-solution aggregates were labeled using a fluorescent additive to directly observe their association/disassociation (using confocal microscopy) during the flow of the polymer through an ordered 2D pore-throat geometry model (Fig. 1A). Furthermore, the macroscopic flow resistance of the SAP and HPAM solutions in the same model were compared to analyze the influence of adaptability on their flow characteristics. All the solutions showed shear thinning followed by shear thickening; the SAP solution behaved differently at the onset of these two stages, exhibiting different viscosity values. Subsequently, a local deformation rate distribution was used to map the local stress distribution, which quantitatively validated the occurrence of association/disassociation. Additionally, the pore-level velocities during multiple-phase flow within a transparent 3D porous medium (Fig. 1B) were monitored using particle image velocimetry (PIV); the SAP and HPAM solutions exhibited different mechanisms of velocity-field change and oil displacement in porous media.

Table 1 The chemical structures and basic parameters of the SAP, HPAM-1, and HPAM-2

Polymer	Chemical structure	Chemical composition	Molecular weight (g mol^{-1})	Overlap concentration (mg L^{-1})
SAP	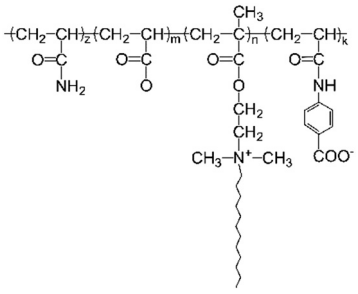	z = 64 mol% m = 26 mol% n = 3 mol% k = 7 mol%	8.7 × 10^6	280
HPAM-1	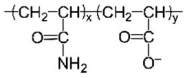	x = 59 mol% y = 41 mol%	8.2 × 10^6	357
HPAM-2	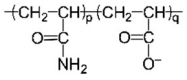	p = 71 mol% q = 29 mol%	24.9 × 10^6	215

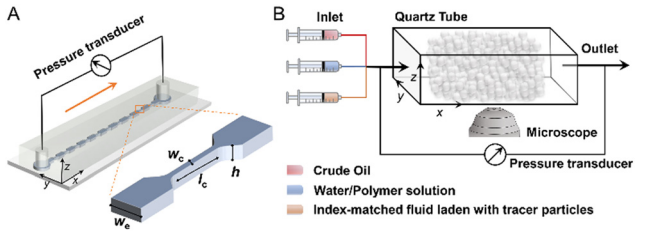

Fig. 1 Schematic diagram of the geometries of the (A) 2D pore-throat model and (B) 3D porous medium, indicating the methods used to measure the pressure drop across the medium and collect images of the flow using a confocal microscope (Experimental).

Results and discussion

Visualizing the association/disassociation of adaptive polymers in solution

In polymers with structures similar to the SAP, hydrophobic supramolecular assemblies form through intermolecular associations of the water-soluble-skeleton hydrophobic side chains above the critical association concentration (CAC).[45] Here, an environment-responsive fluorescence probe, 8-anilino-1-naphthalenesulfonic acid (ANS), was used to directly visualize these hydrophobic aggregates. The water-soluble dye ANS emits a weak fluorescence signal in aqueous solutions and a high-intensity signal in hydrophobic environments.[46,47]

The experimental solutions were analyzed by fluorescence spectroscopy, as shown in Fig. 2A. The fluorescence intensity of the HPAM-1 and HPAM-2 solutions remained unaltered in the entire range of polymer concentrations (C_p) analyzed, with an intensity comparable to that of the dye solution, while low fluorescence intensities was observed at SAP concentrations less than 1000 mg L^{-1} (a concentration that is close to the threshold value of the CAC (854 mg L^{-1}) for the SAP[22]). At SAP concentrations above the CAC, particularly above 2000 mg L^{-1}, the solutions exhibited high fluorescence intensity. Thus, the HPAM aqueous solution was entirely hydrophilic, whereas the SAP solution contained hydrophobic regions. Furthermore, solutions with high polymer concentrations exhibited highly intense fluorescence signals, indicating a large number of hydrophobic microdomains in high-concentration SAP solutions. Additionally, optical images recorded under ultraviolet light (Fig. 2B) indicated that the SAP solutions containing ANS emitted high-intensity fluorescence signals, whereas solutions containing pure ANS, the ANS-free polymer, HPAM-1/ANS, or HPAM-2/ANS were not fluorescent.

Subsequently, the hydrophobic-association aggregates were viewed in the microscale level. In agreement with the spectral results, some areas in the SAP/ANS solution (with a concentration of 1000 mg L^{-1}) exhibited nonuniform fluorescence (Fig. S1†), and a larger number of domains exhibited bright fluorescence on increasing the polymer

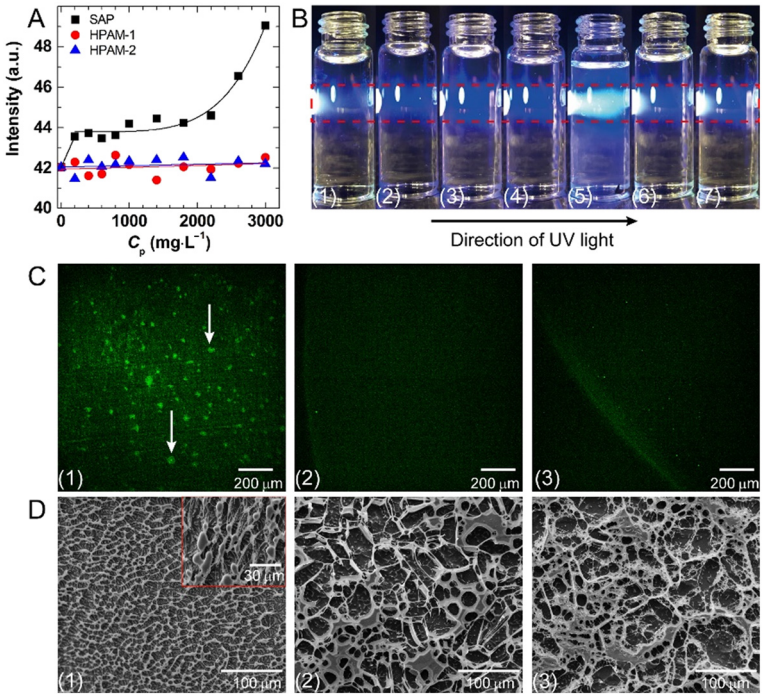

Fig. 2 Characterization of the polymer-solution structure. (A) The variation in the fluorescence intensity *vs.* polymer concentration (C_p), extracted from Fig. S1A–C in the ESI† appendix. (B) Optical images of the ANS B(1), polymer (B(2) SAP, B(3) HPAM-1, and B(4) HPAM-2), and mixture (B(5) SAP/ANS, B(6) HPAM-1/ANS, and B(7) HPAM-2/ANS) solutions under UV light. (C and D) Static confocal and cryo-SEM images of the (1) SAP, (2) HPAM-1, and (3) HPAM-2 solutions with ANS. The excitation wavelength for (A), and (C) is 405 nm. C_p = 3000 mg L^{-1} in (B), (C), and (D). C_{ANS} = 400 mg L^{-1}. T = 22 °C. NaCl solution (4500 mg L^{-1}) is used as the solvent.

concentration to 3000 mg L^{-1} (examples are indicated by arrows in Fig. 2C(1)). Notably, all the HPAM-1 and HPAM-2 solutions emitted low-intensity homogeneous fluorescence originating from the aqueous ANS solution. Subsequently, the dynamic diffusion of ANS in an SAP solution with a concentration of 3000 mg L^{-1} was recorded using a laser confocal microscope (ESI† Movie S1). Areas emitting intense fluorescence gradually appeared on adding the solvent containing ANS to the SAP solution, confirming a local hydrophobic environment in the latter.

The sizes of the SAP-solution fluorescent domains were in the range of 10–40 μm in this study; this is much larger than the previously reported size of hydrophobic microdomains (~8 nm).[48] A previously published quantitative analysis[49] indicates that the number of involved repeat units (N_c) per microdomain depends on the hydrophobic chain length; for instance, the theoretically predicted size of such micelle-like microdomains in an *n*-decyl-containing polysoap ($N_c \approx 14$) is in the order of angstroms. This size is also significantly smaller than the fluorescent-domain size observed here.

To figure out the reason, an independent technique, cryo-SEM, was further used for the direct visualization of the three polymer solutions with a concentration of 3000 mg L^{-1} (Fig. 2D). The SAP solution exhibited a dense and regular network structure connected by numerous nodes with sizes in the range of 5–20 μm, while the two HPAM solutions contained only coarse disorder holes. These results, consistent with those of confocal imaging, confirmed the presence of association aggregates (as the network-structure connecting points) in the SAP solution. Notably, some nodes in the cryo-SEM image of the SAP were in close proximity to each other, which easily causes the fluorescence-signal overlap under a confocal microscope with lower resolution than SEM. This is exactly the reason why enhanced-fluorescence regions of SAP solution observed in this study are significantly larger than the aforementioned reported value.

Further insights into the dynamic adaptive behavior of the aggregates were acquired by observing the flow of the SAP in a 2D pore-throat model containing ten converging–diverging sections. For flow in a wide channel-section, a strip shaped fluorescent patch with a length of ~50 μm was observed under flow resistance (Fig. 3A), which emitted a mean fluorescence intensity of approximately 104–114 (gray value linked to 8 bit pictures). As the flow reached a confined pathway, the fluorescent domain disappeared, and the mean gray value of image decreased to 63. The fluorescent patch reappeared in the next wide region, with the mean gray value increasing to 87. These observations confirmed the *in situ* reversible association/disassociation behavior of the SAPs at the molecular level. As schematically illustrated in Fig. 3B, the ANS molecules dissolved in the hydrophobic domains of the SAP in aqueous solution, emitting a fluorescence signal during the broad-channel flow. Under an elevated applied stress (on passage through the small throat), the weakly interacting hydrophobic aggregates disassembled, disrupting the hydrophobic environment; this

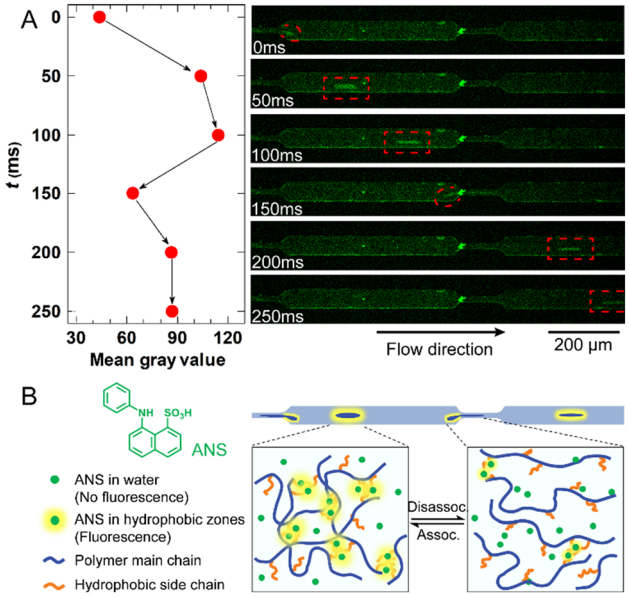

Fig. 3 (A) Confocal images of the SAP/ANS solution at different times in a sample converging–diverging section of the 2D pore-throat model, and the mean gray value of the corresponding fluorescence-enhanced regions. The solution flows at a rate of 2.88 μl h^{-1}. The excitation wavelength is 405 nm. C_p = 3000 mg L^{-1}, C_{ANS} = 400 mg L^{-1}, T = 22 °C, and an NaCl solution (4500 mg L^{-1}) was used as the solvent. (B) Schematic diagram of the association/disassociation process in an SAP-polymer solution flowing through the pore space and throat.

placed the ANS molecules in a polar hydrophilic environment, pausing the fluorescence-intensity enhancement. On re-entering the wide channel (with low shear force), intermolecular hydrophobic association regenerated a hydrophobic environment, re-enhancing the fluorescence intensity.

Quantifying the adaptive-polymer-solution flow behavior in a 2D pore-throat micromodel

To analyze the influence of reversible association/disassociation on the flow characteristics of adaptive polymer solutions in porous media, the SAP, HPAM-1, and HPAM-2 solutions with the same initial apparent shear viscosity (η_0) value of 55 mPa s (the values were made similar by adjusting the operational concentrations of the polymers in solution) were used. All the solutions were maintained at semi-dilute concentrations, with C_{SAP} = 1000 mg L^{-1}, $C_{HPAM\text{-}1}$ = 1300 mg L^{-1}, and $C_{HPAM\text{-}2}$ = 525 mg L^{-1}, based on their overlap concentrations summarized in Table 1.

The pure shear flow was measured by a rotational rheometer with a well-defined geometry. The bulk shear viscosities (η_S) as a function of shear rate ($\dot{\gamma}$) have been represented by open symbols in Fig. 4A. Viscosity reductions in the shear-governed region are driven by polymer-coil disentanglements[5,50–52] and SAP-solution intermolecular disassociations. Thus, the η_S and characteristic shear rate ($\dot{\gamma}_c$) for the onset of shear thinning, evaluated by fitting the experimental data to an empirical model (eqn (1)),[5,53] were

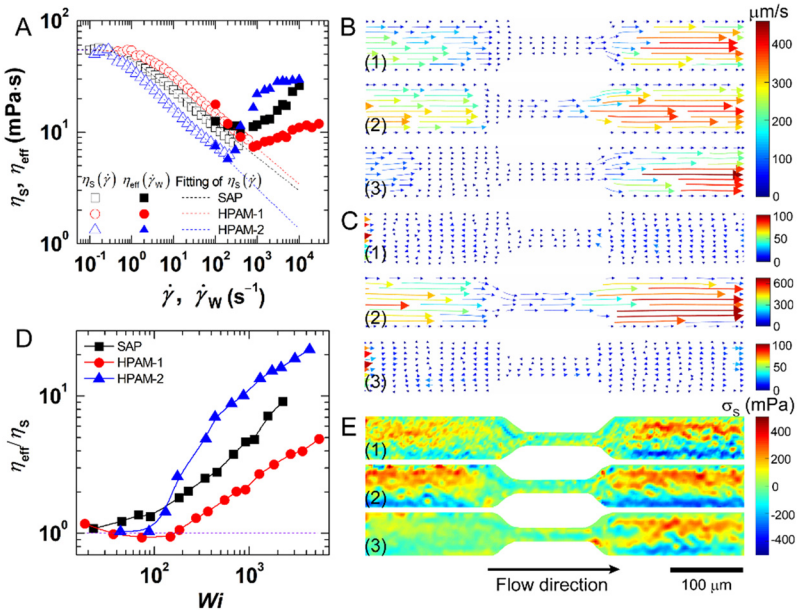

Fig. 4 The macroscopic flow resistance and pore-scale flow characterization of the SAP, HPAM-1, and HPAM-2 solutions at 22 °C. (A) The rheometric depiction in a rotational rheometer where the bulk shear viscosity (η_S) is a function of the shear rate $\dot{\gamma}$ (indicated by open symbols). Above a threshold flow rate, parameterized by the wall shear rate of the narrow channel ($\dot{\gamma}_W$), the effective viscosity (η_{eff}) (indicated by solid symbols) in the 2D pore-throat model abnormally increased and deviated from the predictions of the modified Carreau model for the bulk shear viscosity (dashed lines). (B and C) The flow visualizations in a sample converging–diverging section, for flow rates of 2.88 and 7.2 μl h^{-1}, respectively. Arrows indicate the vector field and colors indicate the magnitude of the average velocity. (D) The reduced viscosity (η_{eff}/η_S) of three polymer solutions in the 2D pore-throat model plotted as a function of the Weissenberg number (Wi). (E) Heat maps of shear stress (σ_S) in the corresponding 2D plane. The negative sign of the stress value represents *a* direction that is opposite to that of a positive value in (B), (C), and (E), where (1), (2), and (3) represent the results for the SAP, HPAM-1, and HPAM-2 solutions, respectively. C_{SAP} = 1000 mg L^{-1}, C_{HPAM-1} = 1300 mg L^{-1}, and C_{HPAM-2} = 525 mg L^{-1} in the NaCl solution (4500 mg L^{-1}) to maintain a similar initial viscosity.

used to compare the molecular-level flow behaviors of the three polymer solutions.

$$\eta_S = \frac{\eta_0}{\left[1 + (\dot{\gamma}/\dot{\gamma}_c)^2\right]^{1-n/2}} \quad (1)$$

The $\dot{\gamma}_c$ value of the SAP (0.56 s^{-1}) was higher than that of HPAM-2 (0.34 s^{-1}), and significantly lower than that of HPAM-1 (2.00 s^{-1}), characterizing that the disruption of entangled structures of HPAM-2 high-MW chains followed by the disassociation and disentanglement of SAP polymer chains on increasing the shear rate beyond $\dot{\gamma}_c$, while the intertwined framework of the HPAM-1 solution was the most difficult to disrupt. Thus, the $\eta_S(\dot{\gamma}_W)$ of the HPAM-1 solution in the entire shear-thinning region was greater than those of the SAP and HPAM-2 solutions. The HPAM-2 solution was more elastic than the SAP and HPAM-1 solutions in the shear-thinning regime, exhibiting the longest relaxation time (437 ms) among the three polymers, as summarized in Table S1.†

Subsequently, the macroscopic flow behaviors of the three polymer solutions in a 2D pore-throat model were analyzed by plotting their effective viscosity, η_{eff}, (Materials and methods) against the wall shear rate, $\dot{\gamma}_W$, of the constricted sections, as shown in Fig. 4A (solid symbols). At low flow rates, the η_{eff} was almost equal to the bulk shear viscosity, *i.e.*, $\eta_{eff}(\dot{\gamma}_W) \approx \eta_S(\dot{\gamma}_W)$; however, it increased when the flow rate exceeded a critical $\dot{\gamma}_W$ value ($\dot{\gamma}_{W,c}$; 800, 1000, and 300 s^{-1} for the SAP, HPAM-1, and HPAM-2 solutions, respectively). This is consistent with the pressure-drop data shown in Fig. S3.† Although this anomalous increase in macroscopic flow resistance is broadly consistent with previous reports on conventional polymer solutions,[10,43,54] the intricacies of the adaptive-polymer-solution behavior are unique. The SAP solution exhibited an onset of viscosity enhancement at a smaller $\dot{\gamma}_{W,c}$ value compared to that exhibited by the HPAM-1 solution, despite similar η_0 values. Furthermore, the high-MW HPAM-2 solution exhibited flow thickening at the lowest flow rate among all the polymer solutions.

To elucidate the anomalous thickening behavior observed, the local pore-scale fluid velocities were analyzed using two flow rates (corresponding to the $\dot{\gamma}_W$ values of 400 and 1000 s^{-1}). On injecting the SAP and HPAM-1 solutions at low flow rates (where the shear force dominates), steady laminar flow patterns and symmetric velocity profiles were generated, possibly due to the low viscous drag of the polymer solutions in the end-piece (in the range of flow thinning) (Fig. 4B and ESI† Movie S2). On injecting the HPAM-2 solution, some curved flowlines were observed in the upstream entrance, consistent with recent numerical simulation predictions.[14] Notably, along with an abnormal increase in flow resistance, the SAP and HPAM-2 solutions showed intense spatial and temporal fluctuations at

high flow rates, as shown in Fig. 4C and ESI† Movie S3, and the fluid streamlines persistently crossed and veered over time, indicating elastic instability. The HPAM-1 solution maintained steady flow, possibly because the $\dot{\gamma}_W$ value was lower than the critical shear rate of the solution for flow instability.

Above visualizations indicated that the flow-thickening onset coincided with the onset of flow fluctuations, and first occurred upstream; this is in agreement with previous reports for both polymer[13,55–59]and viscoelastic surfactant[41,60] solutions, which attribute the thickening behavior to the viscous dissipation arising from the elastic instabilities.

Furthermore, the pore-scale transition from laminar flow to the elastic-dominated regime was analyzed using the nondimensional Weissenberg number (Wi), representing the ratio of elastic to viscous stress, expressed as the ratio of the characteristic relaxation time (λ) of the fluid to that of the porous medium ($1/\dot{\gamma}_W$). Fig. 4D shows the reduced viscosity of the polymer solution, η_{eff}/η_S, as a function of the Wi value. The two HPAM solutions exhibited $\eta_{eff}/\eta_S \approx 1$ at low values of Wi, consistent with their η_{eff} *vs.* $\dot{\gamma}_W$ profiles. At higher values of Wi (>100), the η_{eff}/η_S consistently increased due to the development of an unstable flow. Although this critical Wi value (Wi_c) is significantly higher than those obtained by 3D-disorder-medium analyses,[13] it is consistent with values reported in prior studies on non-adaptive polymers in 2D media.[16,17]

The SAP exhibited a small Wi_c, indicating an additional flow resistance in the SAP solution before the onset of unstable flow. Subsequently, the properties of the SAP and HPAM-1 solutions, with similar MW and initial viscosity values, were compared. The former exhibited a larger η_{eff}/η_S value than the latter, contrary to the trend exhibited by their shear viscosity values, yet similar to that exhibited by their extensional viscosity values (measured by a rheometer in a previous publication[22]). This confirmed the extensional resistance of the associated structure to be an extra flow resistance. To be specific, in domains with $\dot{\gamma}_W > \dot{\gamma}_{W,c}$, the channel contraction/expansion characteristics would induce molecular-level polymer-chain deformations along the flow.[55,61–63] This stretches the polymer coil along the channel, especially while flowing across a narrow channel under a high shear rate. Thus, molecular-chain elastic deformations predominate the orientation and slippage.

Summarizing, although the adaptive polymer showed the same instability as the non-adaptive polymers, the onset of viscoelastic-governed flow for the SAP was more rapid than that of the similar-MW HPAM-1, but slower than that of the ultrahigh-MW HPAM-2, with increasing the flow rate. The earlier onset of elastic instability in the SAP solution compared to the HPAM-1 solution could be attributed to the denser network structure of the SAP, as indicated by cryo-SEM images. Owing to having high MW, the individual polymer chain of HPAM-2 is longer than that of SAP and HPAM-1, which facilitates the occurrence of intrachain entanglement even in the low-concentration regime.[50,64] This fact thus causes an elastic deformation and a flow-arresting fluctuation in HPAM-2 flow, even in the early stages of flow thickening. Moreover, apart from the common viscous dissipation arising from flow fluctuations, the resistance of the supramolecular-association structure of the adaptive polymer to stretching also facilitated flow thickening.

Subsequently, the macroscopic resistances and velocity vectors were extrapolated to the corresponding stress values, to analyze the occurrence of association/disassociation. The SAP-solution intermolecular association/disassociation was mainly influenced by the shear force; thus, the local tangential stress was mapped only at $\dot{\gamma}_W = 400\ s^{-1}$ (the same conditions as in the visually confocal observation before), where the three polymer solutions exhibited linearly stable flow. Mathematically, the stress is represented by $\sigma = \eta\left(\pm\frac{du}{dy}\right)$, where η is the deformation rate-dependent viscosity, and $\frac{du}{dy}$ denotes the velocity gradient, *i.e.*, the shear rate. Then by applying the shear-viscosity equations ($\eta_S - \dot{\gamma}$) and $\dot{\gamma}$ distribution (Fig. S4†) obtained before to stress expression, the local shear stresses (σ_S) for three polymer solutions in a sample converging–diverging section were estimated and shown in Fig. 4E. In the upstream direction, the σ_S value of the HPAM-2 solution was significantly lower than those of the SAP and HPAM-1 solutions, possibly due to flow fluctuations (considering the flow velocity and direction) in the high-MW polymer solution (see ESI† Movie S2). Downstream, due to similar viscosities, lesser differences were observed between the flows of the three polymer solutions; the profiles for all polymer solutions were symmetrically distributed along the centerline, with a maximum shear stress (~400 mPa) near the wall, in agreement with theoretical predictions based on channel geometry.[65]

On the basis of these forces per unit surface area (unit, Pa≡N m^{-2}), the energy of polymer suffering from porous media over the entire volume of fluid was computed using $U \equiv \int_v \sigma_{ij} dV$, where σ_{ij} is the normal or tangential component of the applied stress tensor. Unfortunately, the exact U value can be assessed only from a full 3D velocity field, which is outside the scope of this study. Alternatively, the U of the SAP polymer molecules in a 2D plane were analyzed using the channel dimensions and average stress (measured by the maximum value of the shear stress in the wide channel). Notably, the energy in an expansion section (U_e) of model was ~10^{-12} N m≡J. By applying $\dot{\gamma}_W = 2Q/Aw_c$ and $w_e/w_c = 5$ (Experimental) with $\sigma_S \propto \eta_S(\dot{\gamma}_W)\cdot\dot{\gamma}_W$, the approximate value of energy for the SAP solution in a constriction channel was evaluated, $U_c \approx 10^{-11}$ J. Subsequently, considering the molar content of the polymer, the energy applied to one mole of the SAP polymer in the contraction channel was estimated to be ~200 kJ mol^{-1}, larger than the energy of noncovalent hydrophobic interactions (<100 kJ mol^{-1}), supporting the occurrence of disassociation; meanwhile, this energy value is lower than the C–C bond breakage energy (346 kJ mol^{-1}), which confirms the absence of polymer-backbone disruption during supramolecular-aggregate disassociation. In this case, the association structure can reform when the polymer solution flows through a low stress zone.

Scaling the adaptive polymer-induced velocity distribution change in a 3D micromodel

The flow description in a 2D pore-throat model excludes some vital features of practical applications, namely, medium complexity and the presence of multiple phases, which cause flow-distribution spatial heterogeneity.[11,13,43] Therefore, in this study, multi-phase flow (including oil saturation, initial water displacement, polymer solution flooding, and chase water flushing) was implemented within a 3D porous medium. After each flooding sequence, the remaining oil distribution was imaged using a confocal microscope, and an index-matching solution with a refractive index similar to that of glass beads was used to map the velocity field using PIV (Experimental) for an analysis of any polymer-induced accessible pore-space changes.

As shown in Fig. 5A–C, significant polymer-induced velocity changes (by more than a factor of four) were observed across the 3D porous medium. In the HPAM polymer solutions, the pore-level velocities after chase water injection were significantly higher than the velocity after the initial water displacement. This is consistent with a previously published result[66] indicating due to polymer retention. Notably, the flow velocities of most of the pores remained unchanged or decreased during the SAP-solution flow after the polymer and water injections.

To quantify the local-velocity variation, the probability density functions (PDFs) of the velocity magnitudes after the three displacement procedures were compared. As shown in Fig. 5D–F, the velocity magnitudes of all the groups were broadly distributed, especially after SAP-solution injection. All the PDFs exhibited a nearly exponential decay with varying characteristic speeds, unlike the single decay rate reported in the literature.[11,66] Additionally, polymer-induced PDF changes were mainly observed for $u > 10$ μm s^{-1}; this is approximately 1.25 times greater than the average interstitial velocity, $u_{int} = Q/(A\phi_0)$, of the 3D medium used (8 μm s^{-1}).

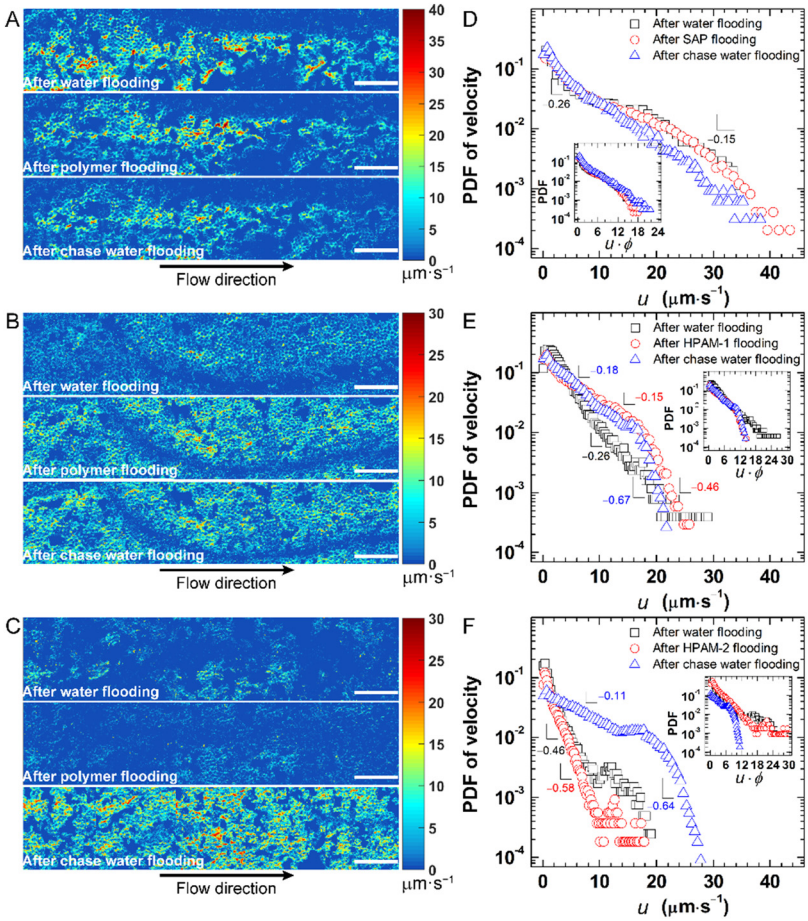

Fig. 5 Scaling of the polymer-induced velocity distribution change during multi-phase displacement in a 3D micromodel at 22 °C. (A–C) Heat maps of the fluid-velocity magnitude in a 2D plane within the 3D porous medium, at a flow rate of 100 μl h^{-1} after water flooding, after polymer injection, and after chase water flooding for (A) SAP, (B) HPAM-1 and (C) HPAM-2 flooding groups, respectively. The scale bar is 500 μm. (D–F) The probability density functions (PDF) of the flow velocities after water, polymer, and chase water flooding are represented by black squares, red circles, and blue triangles for the (D) SAP, (E) HPAM-1, and (F) HPAM-2 solutions, respectively. The insets show the scaling behavior on normalizing the velocities by $1/\phi$. C_{SAP} = 1000 mg L^{-1}, $C_{HPAM\text{-}1}$ = 1300 mg L^{-1}, and $C_{HPAM\text{-}2}$ = 525 mg L^{-1}, to maintain a similar value of initial viscosity in an NaCl solution (4500 mg L^{-1}).

According to a previous publication,[66] the permeability reduction and pore-level velocities are correlated and can be scaled using $u \propto 1/\sqrt{k}$ in the two-phase flow of a water/polymer solution. However, the exact permeability value could not be obtained using Darcy's law due to multi-phase flow in this study. Therefore, the Kozeny–Carman relation $\left(k = \frac{1}{45}\frac{\phi^3 R^2}{(1-\phi)^2}\right)$ was used to determine the permeability of the 3D porous medium, where ϕ is the porosity. The medium containing glass beads with R = 19 μm yielded k_0 = 1.59 μm^2, which is close to the value obtained by experimentation (Table S2†). Subsequently, the effective permeability was evaluated using the modified ϕ (calculated from the measured average interstitial velocity) and used to normalize the velocities by $1/\sqrt{k}$, as shown in Fig. S9.† Unfortunately, all the scaled values deviated from one another, inconsistent with previously published results.[66] This deviation indicated that the permeability change due to polymer retention was not the only factor influencing the interstitial-velocity variation of the pores.

As the average interstitial velocity is inversely proportional to porosity at a given volumetric flow rate, the PDFs of the velocities were accurately scaled by $1/\phi$ (highlighted in the inset of Fig. 5D–F). Notably, the curves, especially those of the SAP-flooding group, overlapped with one another, except for a slight deviation in the tail caused by the additional uncertainty of PIV analysis. This scaling behavior confirmed that the velocity alteration during multiple-phase flow originated from the porosity change, *i.e.*, the variation in the accessible pore space. Thus, differences in the velocity fields of the SAP and HPAM displacement groups could be attributed to the reversible association/dissociation behavior of the SAP during propagation in the pores; this increased the accessible pore volume and decreased the possibility of plugging, lowering the interstitial velocity of the pores. However, in the flooding group of the HPAM solutions, particularly in the ultrahigh-MW HPAM-2 group, the velocity magnitude increased significantly and the velocity distribution widened, indicated a significant reduction in the accessible pore volume, possibly because of polymer-molecule clogging (due to its larger hydrodynamic radius (287.2 nm) than SAP (106.7 nm) and HPAM-1 (108.9 nm)[22]). Additionally, after polymer and water injections, the quantity of remaining crude oil (red zone in Fig. S10B–D†) decreased significantly in the SAP-flooding system, and slightly for the HPAM solutions. The release of crude oil relaxed the pores and induced a slight velocity reduction.

Experimental

Preparation and characterization of the bulk polymer solutions

The SAP polymer was synthesized in our laboratory, while HPAM-1 and HPAM-2 were supplied by the Daqing Oilfield Company, China. Their architectures and structural parameters have been characterized in a previous publication[22] and are summarized in Table 1. According to calculations by Zhu *et al.*,[45] an addition of NaCl (0.02 M) is sufficient to screen the ionic strength of a polyelectrolyte with a degree of hydrolysis (DH) of 44% at a polymer concentration of 1 wt%. The SAP, HPAM-1, and HPAM-2, with DH values of 34%, 41%, and 29%, respectively, could be screened by an NaCl solution with a concentration of 4500 mg L^{-1} (≈0.08 M) in this study, and were flexible in solution.

To prepare ANS-containing solutions, NaCl (Sigma–Aldrich, USA) and ANS (VWR, USA) were dissolved in ultrapure Millipore water and passed through a 0.2 μm Millipore filter; subsequently, specific amounts of polymer powders (purified through dialysis and freeze drying) were dissolved in the dyed solvent. The final solution containing the polymer, NaCl (4500 mg L^{-1}), and ANS (400 mg L^{-1}) was filtered with a cell strainer (40 μm) prior to use. Another undyed polymer solution was prepared with the same NaCl content following an identical procedure for use as a control. All the solutions were used within 1 month of preparation.

To characterize the dyed polymer solutions, their fluorescence emission spectra at different concentrations were measured using a Cary Eclipse fluorescence spectrophotometer (Agilent Technologies, USA) under an excitation wavelength of 405 nm. The polymer solutions were transferred to a 5 mL glass bottle and irradiated with a UV lamp in *a* direction perpendicular to the bottle. Subsequently, fluorescence images of the polymer solutions were observed using a confocal microscope (Leica, Germany) under an excitation wavelength of 405 nm. Cryo-SEM images of the polymer solutions were acquired on a scanning electron microscope (SEM) (Quanta 450, FEI, USA) combining cryogenic preparation and transmission systems (PP3000T, Quorum, UK).

The rheological properties of the bulk polymer solutions were evaluated at room temperature (22 °C) using a DHR-3 rheometer (TA, USA) with a 60 mm parallel-plate geometry (Peltier plate Steel) and 1 mm gap. Under steady shear (represented by open symbols in Fig. 4A), the viscosity function could be described well by the modified Carreau model (eqn (1)). The viscoelasticity of the polymer solution was characterized by its stress relaxation response at a strain γ of 10%. The shear-stress variation over time (Fig. S2†) exhibited a good fit to the standard linear solid model:[67]

$$\sigma_S = \gamma(E_1 + E_2 \cdot e^{-t/\lambda}) \quad (2)$$

This equation was used to determine the relaxation time (λ) required by the three polymer-solution chains to return to their equilibrium configuration after disruption, as summarized in Table S1.† E_1 and E_2 indicate the moduli of the two linear spring elements.

Single-phase flow in a 2D pore-throat micromodel

The 2D microfluidic (Fig. 1A) model used, consisting of ten diverging and converging physical constraints (to mimic a

pore body and throat chips), was composed of polydimethyl siloxane (PDMS, Sylgard 184, Dow Corning, USA) and fabricated using the soft lithography method.[43,68] Each contraction-expansion part exhibited the following geometric parameters: an upstream channel width (w_e) of 50 μm, downstream access width (w_c) of 10 μm, uniform length-width ratio of both sections (l/w = 10), and identical channel depth (h) of 40 μm. Additionally, the PDMS chip was cut, punched, cleaned, and finally sealed to a microscope slide by plasma treatment. Before each experiment, the internal channel was coated with Aquapel (Rider, USA) to make the PDMS surface and glass plate highly hydrophobic.

Saline water (an NaCl solution with a concentration of 4500 mg L^{-1}) or a polymer solution was injected into the 2D pore-throat model over a broad range of volumetric flow rates (Q) using a syringe pump (Harvard Apparatus PHD 2000). The sequence was continued until the pressure drop (ΔP) across the whole channel stabilized, as recorded by a differential pressure transducer (Omegadyne PX409, USA). The wall shear rate ($\dot{\gamma}_W$) in the narrow channel, as a reference for the apparent deformation rate, was evaluated by $\dot{\gamma}_W = 2Q/Aw_c$, where A = 400 μm^2 indicates the cross-sectional area of the narrow channel. Varying the value of Q from 0.72 to 216 μl h^{-1} produced a wide range of $\dot{\gamma}_W$ values (spanning 2 orders of magnitude). The Reynolds number, comparing the inertial and viscous stresses, is defined as Re = $\rho(Q/w_c h)D_h/\eta_0$ in this channel,[16,17] where ρ is the density of the fluid, and $D_h = 2w_c h/(w_c + h)$ is the hydraulic diameter of the contraction. In this study, the Re varied in the range of 10^{-4} to 1.2, indicating a predominance of the viscous stress over the inertial stress. Thus, the flow was described using Darcy's law, $\Delta P = \eta Ql/(Ak)$, where ΔP exhibits a positive correlation with the fluid dynamic viscosity (η) under similar conditions. The *in situ* effective viscosity (η_{eff}) of the polymer solution at different flow rates was estimated using $\Delta P_p/\Delta P_w = \eta_{eff}/\eta_w$, where ΔP_p and ΔP_w denote the pressure drop during polymer injection and brine flow, respectively, and η_w = 0.99 mPa s is the viscosity of brine, independent of the shear rate.

To map the pore-scale deformation rate distribution, the polymer solution was seeded with 1 μm-diameter fluorescent polystyrene particles (0.02 vol%) (Invitrogen, USA); the tracer particles exhibited excitation and emission peaks at 505 and 515 nm, respectively. The final system was pumped into the model at a constant flow rate for at least 2 h to equilibrate the solution before flow characterization. Particle diffusion was negligible at the flow rates used here because advection dominated over diffusion, as indicated by the Péclet number, Pe ≡ 10^5–$10^6 \gg 1$. Subsequently, an xy position was selected in a fixed focal z plane, and numerous images were recorded in sequence using confocal microscopy (10× lens, NA = 3, Leica SP5, USA) at a temporal resolution of 15 ms intervals per frame; each image spanned a lateral area of 517 × 63 μm^2. Analyzing these images by the PIVlab program,[69] the local distributions of the shear rate were evaluated, as shown in Fig. S4.†

Multiple-phase flow measurements in 3D porous media

To prepare 3D porous media, borosilicate glass beads (Mo-Sci, USA) with an average radius (R) of 19 μm were densely packed into a square quartz tube (VitroCom, USA) with a cross-sectional area (A_{tube}) of 3 × 3 mm^2 and length (l_{tube}) of ~3 cm, and sintered at 875 °C for 3 min. Subsequently, the inlet and outlet tubing were glued into the ends of the packing medium on a microscope slide, as shown in Fig. 1B. The porosity and permeability values of this disordered granular packing were $\phi \approx 37\%$ and $k \approx 1.4$ μm^2, respectively (see details in ESI†).

Before experimentation, air bubbles were removed under vacuum, followed by a saturation of the medium with gaseous carbon dioxide (which was soluble in the fluid). The device was first filled with crude oil (Daqing Oilfield, China), which was diluted using kerosene at a mass ratio of $w_{oil}:w_{ker}$ = 3 : 2, and exhibited a shear rate-independent viscosity of ~13 mPa s (Fig. S7†). Subsequently, multiphase displacement experiments were conducted by sequentially injecting saline water, the polymer solution (~5 pore volumes), and saline water (again) at 200 μl h^{-1}. The dynamic configurations of the oil and displacing fluid in the medium were monitored using confocal microscopy, as shown in ESI† Movies S4–S6.

To quantify the pore-scale velocities, a mixture of 87.5 vol% dimethyl sulfoxide (Sigma–Aldrich, USA) and 12.5 vol% water, exhibiting the same refractive index as glass beads, was formulated. This index-matched fluid containing fluorescent microparticles (0.005 vol%) was pumped into the medium at a rate of 100 μl h^{-1} after each flooding subsequence. Previous publications indicate that particles at such low dosages and flow rates are reliable streamline tracers.[11,66] Movies were recorded at 2000 frames, at 15 Hz, in a stationary position with a lateral area of 911 × 911 μm^2. Using PIV, the average pore-level velocity in the picture plane was determined at a resolution of 4 × 4 μm^2.[11,66] For a large scale flow visualization, this procedure was repeated at multiple consecutive x positions, and the resulting velocity maps were stitched.

Conclusions

Concluding, this study investigated the flow behavior of adaptive polymer solutions in porous media. The reversible association/disassociation processes of an adaptive polymer in a transparent microfluidic chip (mimicking successive pore throats/bodies in 3D porous media) were directly observed using a fluorescent dye. In contrast to non-adaptive polymer solutions, the autonomous behavior of adaptive polymer solutions impaired the shear-flow resistance of the solution, generating an additional extension-induced flow resistance. Therefore, unlike long-chain polymer solutions, the adaptive polymer solution modified the pore size by increasing the accessible pore space during immiscible-phase displacement, instead of blocking the pores and diverting the flow. Furthermore, an imposed-stress distribution mapping during polymer-solution flow confirmed the occurrence of

association/disassociation. This paper could guide future studies on the physics of the flow and transport of weakly interacting polymer solutions through complicated and realistic porous media. Adaptive polymers exhibit high potential for the expulsion of trapped nonaqueous liquids from reservoirs during groundwater remediation and enhanced oil recovery; this study could facilitate their design and development, contributing immensely to academic and industrial research.

Author contributions

Yan Zhang: conceptualization, methodology, investigation, validation, formal analysis, visualization, writing–original draft. Xuezhi Zhao: investigation, methodology, formal analysis. Peihui Han: resources, formal analysis. Tianlei He: software, visualization. Hongyao Yin: formal analysis. Liyuan Zhang: methodology, software, writing–review & editing. Yujun Feng: conceptualization, supervision, writing-review & editing, funding acquisition. David A. Weitz: resources, supervision, writing-review & editing.

Conflicts of interest

There are no conflicts to declare.

Acknowledgements

This work was funded by the National Natural Science Foundation of China (grant number U1762218). Additionally, Y.Z. acknowledges the China Scholarship Council (CSC) for financial support while visiting Harvard University for two years.

References

1 A. Bourgeat, O. Gipouloux and E. Marusic-Paloka, *Multiscale Model. Simul.*, 2003, **1**, 432–457.
2 M. Luo and I. Teraoka, *Macromolecules*, 1996, **29**, 4226–4233.
3 Q. Xu, M. Hashimoto, T. T. Dang, T. Hoare, D. S. Kohane, G. M. Whitesides, R. Langer and D. G. Anderson, *Small*, 2009, **5**, 1575–1581.
4 A. Dotivala, K. Puthuveetil and C. Tang, *Polymers*, 2019, **11**, 294.
5 G. Chauveteau and K. S. Sorbie, in *Basic concepts in enhanced oil recovery processes*, ed. M. Baviere, Elsevier, 1991, pp. 43–87.
6 A. Skauge, N. Zamani, J. G. Jacobsen, B. S. Shiran, B. Al-Shakry and T. Skauge, *Colloids Interfaces*, 2018, **2**, 1–27.
7 M. M. Smith, J. A. Silva, J. Munakata-Marr and J. E. McCray, *Environ. Sci. Technol.*, 2008, **42**, 9296–9301.
8 T. F. AI-Fariss, *Ind. Eng. Chem. Res.*, 1990, **29**, 2150–2151.
9 F. W. Smith, *JPT, J. Pet. Technol.*, 1970, **22**, 148–156.
10 F. Durst, R. Haas and B. U. Kaczmar, *J. Appl. Polym. Sci.*, 1981, **9**, 3125–3149.
11 S. S. Datta, H. Chiang, T. S. Ramakrishnan and D. A. Weitz, *Phys. Rev. Lett.*, 2013, **111**, 064501.
12 S. Parsa, E. Santanach-Carreras, L. Xiao and D. A. Weitz, *Phys. Rev. Fluids*, 2020, **5**, 022001.
13 C. A. Browne and S. S. Datta, *Sci. Adv.*, 2021, **7**, eabj2619.
14 M. Kumar, S. Aramideh, C. A. Browne, S. S. Datta and A. M. Ardekani, *Phys. Rev. Fluids*, 2021, **6**, 033304.
15 P. L. J. Zitha, G. Chauveteau and L. Léger, *J. Colloid Interface Sci.*, 2001, **234**, 269–283.
16 Z. Li, X. Yuan, S. J. Haward, J. A. Odell and S. Yeates, *J. Non-Newtonian Fluid Mech.*, 2011, **166**, 951–963.
17 S. J. Haward, Z. Li, D. Lighter, B. Thomas, J. A. Odell and X.-F. Yuan, *et al.*, *J. Non-Newtonian Fluid Mech.*, 2010, **165**, 1654–1669.
18 X. Fan, J. Y. Chung, Y. X. Lim, Z. Li and X. J. Loh, *ACS Appl. Mater. Interfaces*, 2016, **8**, 33351–33370.
19 S. Samanta, S. Kim, T. Saito and A. P. Sokolov, *J. Phys. Chem. B*, 2021, **125**, 9389–9401.
20 J. Hu, *Adaptive and functional polymers, textiles and their applications*, World Scientific, 2011.
21 M. D. Das, *J. Pet. Sci. Eng.*, 2018, **170**, 40–48.
22 Y. Zhang, Y. Feng, B. Li and P. Han, *Fuel*, 2019, **251**, 136–146.
23 J.-M. Lehn, *Chem. Soc. Rev.*, 2007, **36**, 151–160.
24 J.-M. Lehn, in *Constitutional dynamic chemistry*, ed. M. Barboiu, Springer, 2012, pp. 1–32.
25 J.-M. Lehn, *Angew. Chem., Int. Ed.*, 2015, **54**, 3276–3289.
26 A. Walther, *Adv. Mater.*, 2020, **32**, 1905111.
27 K. Kalaitzidou and A. J. Crosby, *Appl. Phys. Lett.*, 2008, **93**, 041910.
28 C. Neikirk, *PhD thesis*, Princeton University, 2015.
29 J. A. Kaitz, C. M. Possanza, Y. Song, C. E. Diesendruck, A. J. H. Spiering, E. W. Meijer and J. S. Moore, *Polym. Chem.*, 2014, **5**, 3788–3794.
30 Y. Sagara, H. Traeger, J. Li, Y. Okado, S. Schrettl, N. Tamaoki and C. Weder, *J. Am. Chem. Soc.*, 2021, **143**, 5519–5525.
31 N. Roy, B. Bruchmann and J.-M. Lehn, *Chem. Soc. Rev.*, 2015, **44**, 3786–3807.
32 W. Wang, Z. Zeng, L. Xiang, C. Liu, D. Diaz-Dussan, Z. Du, A. B. Asha, W. Yang, Y.-Y. Peng, M. Pan, R. Narain, J. Liu and H. Zeng, *ACS Nano*, 2021, **15**, 9913–9923.
33 A. Wolfel, C. I. A. Igarzabal and M. R. Romero, *Eur. Polym. J.*, 2020, **140**, 110038.
34 N. Sreenivasachary and J.-M. Lehn, *Proc. Natl. Acad. Sci. U. S. A.*, 2005, **102**, 5938–5943.
35 S. Ulrich and J.-M. Lehn, *J. Am. Chem. Soc.*, 2009, **131**, 5546–5559.
36 I. Luzinov, S. Minko and V. V. Tsukruk, *Prog. Polym. Sci.*, 2004, **29**, 635–698.
37 D. B. Varshey, J. R. G. Sander, T. Friščić and L. R. MacGillivray, in *Supramolecular chemistry: from molecules to nanomaterials*, ed. P. A. Gale and J. W. Steed, Wiley, 2012, pp. 9–24.
38 J. E. Huheey, E. A. Keiter and R. L. Keiter, *Inorganic chemistry*, HarperCollins College Publishers, 1993.
39 A. Anbari, H.-T. Chien, S. S. Datta, W. Deng, D. A. Weitz and J. Fan, *Small*, 2018, **14**, 1703575.

40 C. A. Browne, A. Shih and S. S. Datta, *Small*, 2019, **16**, 1903944.
41 J. J. Cardiel, A. C. Dohnalkova, N. Dubash, Y. Zhao, P. Cheung and A. Q. Shen, *Proc. Natl. Acad. Sci. U. S. A.*, 2013, **110**, E1653–E1660.
42 S. J. Haward, C. C. Hopkins and A. Q. Shen, *Proc. Natl. Acad. Sci. U. S. A.*, 2021, **118**, e2111651118.
43 G. Chauveteau and M. Moan, *J. Phys., Lett.*, 1981, **42**, 201–204.
44 L. Choplin and J. Sabatié, *Rheol. Acta*, 1986, **25**, 570–579.
45 R. Zhu, Y. Feng and P. Luo, *Macromolecules*, 2020, **53**, 1326–1337.
46 D. Ito and H. Itagaki, *Eur. Polym. J.*, 2018, **99**, 277–283.
47 T. Matsuda, R. Kawakami, T. Nakajima and J. P. Gong, *Macromolecules*, 2020, **53**, 8787–8795.
48 A. Benjelloun, C. Dorion, A. Brembilla, M.-L. Viriot and M. Adrian, *Macromol. Symp.*, 1998, **127**, 165–171.
49 W. Binana-Limbelé and R. Zana, *Macromolecules*, 1990, **23**, 2731–2739.
50 K. Lewandowska, *J. Appl. Polym. Sci.*, 2007, **103**, 2235–2241.
51 D. A. Z. Wever, F. Picchioni and A. A. Broekhuis, *Prog. Polym. Sci.*, 2011, **36**, 1558–1628.
52 D. W. Mead and R. G. Larson, *Macromolecules*, 1998, **31**, 7895–7914.
53 G. Chauveteau, *J. Rheol.*, 1982, **26**, 111–142.
54 N. Kauser, L. Dos Santos, M. Delgado, A. Muller and A. Saez, *J. Appl. Polym. Sci.*, 1999, **72**, 783–795.
55 D. Kawale, E. Marques, P. L. J. Zitha, M. T. Kreutzer, W. R. Rossen and P. E. Boukany, *Soft Matter*, 2017, **13**, 765–775.
56 P. Pakdel and G. H. McKinley, *Phys. Rev. Lett.*, 1996, **77**, 2459–2462.
57 A. Groisman and V. Steinberg, *Nature*, 2000, **405**, 53–55.
58 D. Samanta, Y. Dubief, M. Holzner, C. Schäfer, A. N. Morozov, C. Wagner and B. Hof, *Proc. Natl. Acad. Sci. U. S. A.*, 2013, **110**, 10557–10562.
59 G. H. Choueiri, J. M. Lopez, A. Varshney, S. Sankar and B. Hof, *Proc. Natl. Acad. Sci. U. S. A.*, 2021, **118**, e2102350118.
60 S. De, S. P. Koesen, R. V. Maitri, M. Golombok, J. T. Padding and J. F. M. van Santvoort, *AIChE J.*, 2018, **64**, 773–781.
61 P.-G. de Gennes, *J. Chem. Phys.*, 1974, **60**, 5030–5042.
62 N. Zamani, I. Bondino, R. Kaufmann and A. Skauge, *J. Pet. Sci. Eng.*, 2015, **133**, 483–495.
63 J. G. Jacobsen, B. S. Shiran, T. Skauge, K. S. Sorbie and A. Skauge, *Polymers*, 2020, **12**, 452.
64 T. Sochi, *Polymer*, 2010, **51**, 5007–5023.
65 J. E. Glass, D. N. Schulz and C. F. Zukoski, *ACS Symp. Ser.*, 1991, **462**, 2–17.
66 S. Parsa, A. Zareei, E. Santanach-Carreras, E. J. Morris, A. Amir, L. Xiao and D. A. Weitz, *Phys. Rev. Fluids*, 2021, **6**, L082302.
67 F. Mainardi and G. Spada, *Eur. Phys. J.: Spec. Top.*, 2011, **193**, 133–160.
68 E. W. M. Kemna, R. M. Schoeman, F. Wolbers, I. Vermes, D. A. Weitz and A. van den Berg, *Lab Chip*, 2012, **12**, 2881–2887.
69 W. Thielicke and E. J. Stamhuis, *PIVlab-time-resolved digital particle image velocimetry tool for MATLAB (version: 2.50)*, Figshare, DOI: **10.6084/m9.figshare.1092508**.

